ECS Journal of Solid State Science and Technology, **2** (2) R3001-R3011 (2013)
2162-8769/2013/2(2)/R3001/11/$28.00 © The Electrochemical Society

JSS Special Issue on Luminescent Materials for Solid State Lighting

A Review on How Lanthanide Impurity Levels Change with Chemistry and Structure of Inorganic Compounds

Pieter Dorenbos[z]

Delft University of Technology, Faculty of Applied Sciences, Department of Radiation Science and Technology, Luminescence Materials Research Group, 2629 JB Delft, Netherlands

The energy of the 4f-5d transitions of divalent and trivalent lanthanide impurities in compounds depends strongly on the type of lanthanide, its valence, and the type of compound. Despite this large variability there is much systematic in 4f-5d transition energy. Once it is known for one lanthanide that for all others when in the same compound can be predicted. The same applies for the energy of electron transfer from the valence band to the 4f-shell of lanthanides which also behaves in a systematic fashion with type of lanthanide and type of compound. This work reviews my studies during the past fifteen years that are based on an analysis of data on all divalent and all trivalent lanthanides in more than 1000 different inorganic compounds collected from the archival literature. The established redshift and charge transfer models that form the basis to construct binding energy schemes showing all lanthanide levels with respect to the host bands are reviewed and the latest developments are addressed.
 [DOI: 10.1149/2.001302jss]

Manuscript submitted July 23, 2012; revised manuscript received August 21, 2012. Published November 27, 2012. *This paper is part of the JSS Special Issue on Luminescent Materials for Solid State Lighting.*

The lanthanide ions are widely used to functionalize inorganic compounds, most noteworthy for phosphor application in lighting and display. To understand the performance of lanthanide activated materials, knowledge on the electronic structure is needed which can be obtained by studying optical transitions. Figure 1 shows as a typical example the emission and excitation spectrum of Tm^{3+} in $LiYP_4O_{12}$.[1] Here we distinguish three different types of transitions as illustrated in Fig. 2. 1) The interband transitions are between the valence band and conduction band states and define the bandgap of the compound. It often appears as a distinct band or strong cutoff at the energy E^{ex} of host exciton creation in lanthanide luminescence excitation spectra. In Fig. 1 the exciton creation is manifest by a cutoff in the Tm^{3+} luminescence excitation spectrum 2) The intra-lanthanide transitions are within one and the same lanthanide, and one may distinguish the intra $4f^n$-$4f^n$ and inter-configurational $4f^n$-$4f^{n-1}5d$ transitions. The $4f^n$-$4f^n$ transitions are narrow and parity forbidden whereas the parity allowed 4f-5d transitions are typically few 0.1 eV wide. Both types can be seen in Fig. 1. 3) The charge transfer transitions are between a lanthanide state and a host band state and they provide information on the location of the lanthanide levels relative to the valence and conduction band. Excitation of an electron from the valence band to the 4f-shell of Tm^{3+} gives the more than 1 eV wide excitation band at 7.8 eV in Fig. 1.

In this review first the systematics in 4f-5d transition energies are presented together with the models describing those systematics. It concerns the redshift models, centroid shift models, and models on the crystal field splitting. Next the electron transfer from the valence band to the 4f-shell of trivalent lanthanides is treated. It forms the basis to construct host referred binding energy schemes (HRBE) that show the binding energy of electrons in all lanthanide impurity states relative to that in the valence and conduction band states. Finally the most recent developments in the modeling of electronic binding energy schemes are presented. The chemical shift model enables to relate the entire HRBE scheme relative to the vacuum energy.

The 4f-5d Transition Energies

Going through the lanthanide series in the periodic table of the elements, the 4f-shell is being filled with electrons from n=1 for La^{2+} and Ce^{3+} to n=14 for Yb^{2+} and Lu^{3+}. The 4f-shell is regarded an inner shell since it is surrounded by filled $5p^6$ and $5s^2$ subshells belonging to the [Xe] electron configuration. With the filling of the 4f-shell the ionic radius of the lanthanide contracts by about 18 pm.[2]

The level spacing's between excited $4f^n$ states are almost entirely controlled by the electron-electron interactions within the 4f-shell. These interactions are very characteristic for a lanthanide ion, and the chemical environment (or the crystal field) has little influence on those level spacing. One may conveniently use the Dieke and Crosswhite diagram of UV-VIS $4f^n$ level spacing's, that was extended to the vacuum ultra violet by Meijerink and co-workers,[4,5] for each inorganic compound.[3]

Figure 3 shows the calculated radial distribution function of the 4f-orbital of Ce^{3+} in BaF_2.[6] It is maximum at 38 pm from the nucleus of Ce^{3+} and it shows small overlap with the 2p wave function of the fluorine ligand. When an electron is excited from the 4f-orbital to the empty 5d-orbital the $[Xe]4f^{n-1}5d$ configuration is obtained. Contrary to the 4f-orbital, the 5d-orbital extends beyond the [Xe] core. In Fig. 3 the 5d-electron wave function has maximum probability density at 108 pm, and it strongly overlaps with the fluorine ligand. This causes that the crystal field interaction with 5d-electrons is about 50 times stronger than with 4f-electrons, and 5d-level energies depend strongly on the type of compound.

When we speak about the 5d-level energy always the binding energy of the electron in that 5d-level with respect to the binding energy of an electron in the $4f^n$ ground state will be meant. For practical reasons the energy of a 5d-level is determined at the maximum of

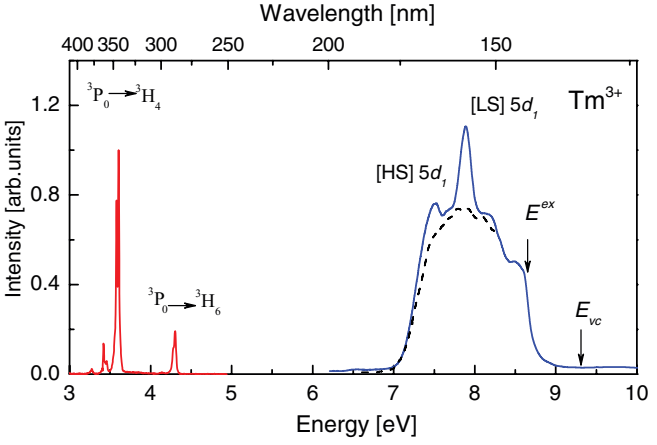

Figure 1. The excitation spectrum of 3.60 eV emission and the emission spectrum under 7.13 eV excitation of Tm^{3+} in $LiYP_4O_{12}$ at 10K. The dashed curve is the predicted location of the CT-band.

[z]E-mail: p.dorenbos@tudelft.nl

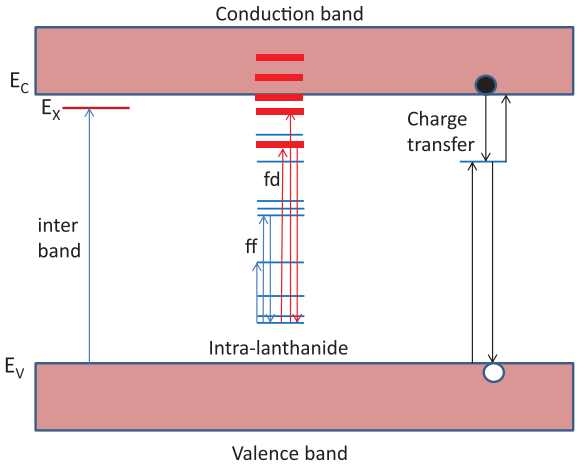

Figure 2. Three different types of electronic transitions in lanthanide activated compounds.

the 4f-5d absorption or excitation band. It therefore refers to the so-called side band maximum and not to the energy of the zero-phonon transition. This review deals exclusively with the 4f-5d excitation or absorption energies and not with 5d-4f emission energy and the Stokes shift. It also deals mostly with trivalent lanthanides. The story on the divalent lanthanides is quite analogous and only the main differences and analogies with the trivalent lanthanides are addressed.

Many data, covering more than 1000 different inorganic compounds, has been collected from the archival literature; not only on 4f-5d transition energies but also on host excitation energies and the energies of charge transfer bands. To handle that data and to visualize trends with composition and structure of the host compound, a 7-digit compound identification number A was introduced in.[7,8] The first two digits group the compounds according to type of anions present (fluorides, chlorides, bromides, iodides, oxides, sulfides, selenides, tellurides, nitrides). The following two digits indicate how the anions are bonded (phosphates, borates, silicates, aluminates), and the last three digits indicate the type of rare earth ion (La, Gd, Y, Lu, Sc), type of divalent cation (Ba, Sr, Ca, Mg), and type of monovalent cation (Cs, Rb, K. Na. Li). Also the names of symbols for energy differences between states were standardized. In $E^{sup}_{sub}(n, Q, A)$ the subscript denotes the initial and final states involved; like fd_1 to denote the energy difference between the 4f ground state and the first 5d state or VC to

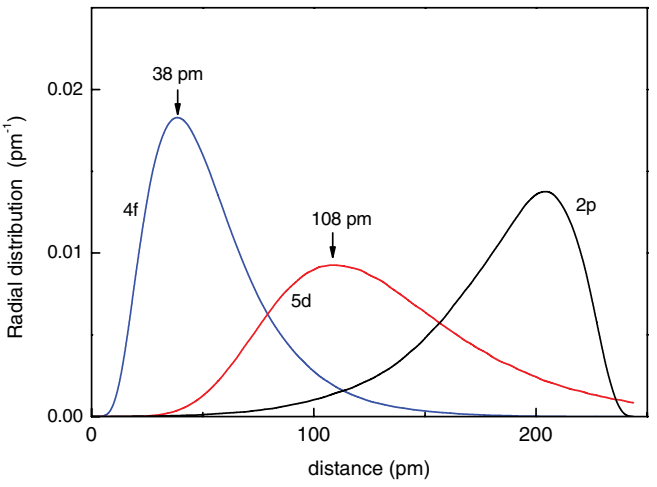

Figure 3. 4f and 5d radial distribution functions of Ce^{3+} and the radial distribution of the 2p wave function of F^- in BaF_2 as calculated from results in Ref. 6.

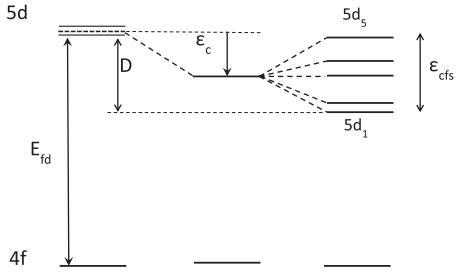

Figure 4. The effect of crystal field splitting and centroid shift on the 5d-level energies of Ce^{3+}.

denote energy difference between valence and conduction band. The superscript indicates the type of transfer; like CT when charge transfer is involved or ex when it concerns the host exciton etc. n is the number of electrons in the 4f-shell before the transition, Q denotes the charge of the lanthanide before the transition, and A represents the compound.

The systematics with type of lanthanide.—The redshift model.— The 4f-5d transitions of Ce^{3+} are the most studied of all trivalent lanthanides for several reasons. Ce^{3+} has only one electron in the 4f-shell leading to most simple 4f-5d excitation spectra. Secondly, the energies of the 4f-5d transitions are the lowest amongst all trivalent lanthanides, and they can be conveniently studied in the UV-VIS part of the spectrum. The interaction between the 5d-electron of Ce^{3+} and the chemical environment affects the level energies as illustrated in Fig. 4. Depending on the point symmetry at the Ce^{3+} site, the spin orbit split $^2D_{\frac{5}{2},\frac{3}{2}}$ terms of the free Ce^{3+} ion are further split into at most five different levels. In addition, the average of the five 5d-level energies shifts toward lower energy. The energy difference between the lowest $5d_1$ and highest energy $5d_5$ level defines the total crystal field splitting $\epsilon_{cfs}(1, 3+, A)$, and the average energy of the five 5d-levels is the centroid energy $E^C(1, 3+, A)$. The centroid shift $\epsilon_c(1, 3+, A)$ is defined as[9]

$$\epsilon_c(1, 3+, A) \equiv 6.35 - E^C(1, 3+, A) \quad [1]$$

where 6.35 eV is the average energy of the 5d-levels in gaseous Ce^{3+}. The combination of crystal field splitting, spin-orbit splitting, and centroid shift leads to a lowering of the $5d_1$ level by an amount that was named the redshift or depression $D(1, 3+, A)$ defined as[10]

$$D(1, 3+, A) \equiv 6.12 - E_{fd_1}(1, 3+, A) \quad [2]$$

where 6.12 eV is the energy of the first 4f-5d transition in gaseous Ce^{3+}.

Figure 5 shows the energy $E_{fd_1}(n, 3+, A)$ for Ce^{3+} ($n = 1$), Pr^{3+} ($n = 2$), and Nd^{3+} ($n = 3$) against $E_{fd}(1, 3+, A)$ when on the same site in the same compound. The data for Ce^{3+} then all fall on a line of unit slope. The data for the free (gaseous) lanthanides are on the far right, and in compounds the energy is lowered by the redshift $D(n, 3+, A)$. Data for Pr^{3+} and Nd^{3+} fall on lines of unit slope parallel to that for Ce which proofs that the redshift is to good approximation the same for all three lanthanides. Similar plots were made for the other lanthanides[10] and one may write $D(n, 3+, A) = D(1, 3+, A) \equiv D(3+, A)$ for all values of n. One may now collect information on the redshift value of any of the trivalent lanthanides and use that to predict the energy $E_{fd_1}(n, 3+, A)$ for all other trivalent lanthanides using

$$E^{s.a.}_{fd_1}(n, 3+, A) = E^{s.a.}_{fd_1}(n, 3+, \text{free}) - \text{D}(3+, \text{A}) \quad [3]$$

where the superscript s.a. means that the first spin allowed 4f-5d transition is considered. $E_{fd_1}(n, 3+, \text{free})$ is the energy extrapolated from graphs as in Fig. 5 toward the point of zero redshift. A first set of $E_{fd_1}(n, 3+, \text{free})$ values was presented in.[10] With time more and

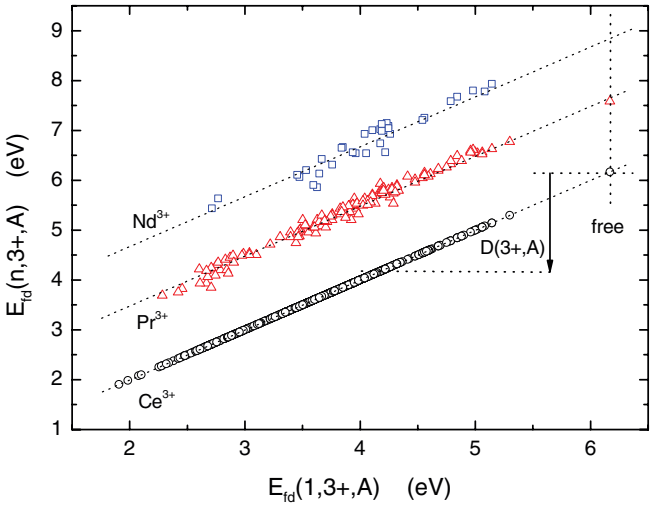

Figure 5. Energy of the first 4f-5d transition for Ce^{3+}, Pr^{3+} (199 compounds), and Nd^{3+} (40 compounds) against that for Ce^{3+}.

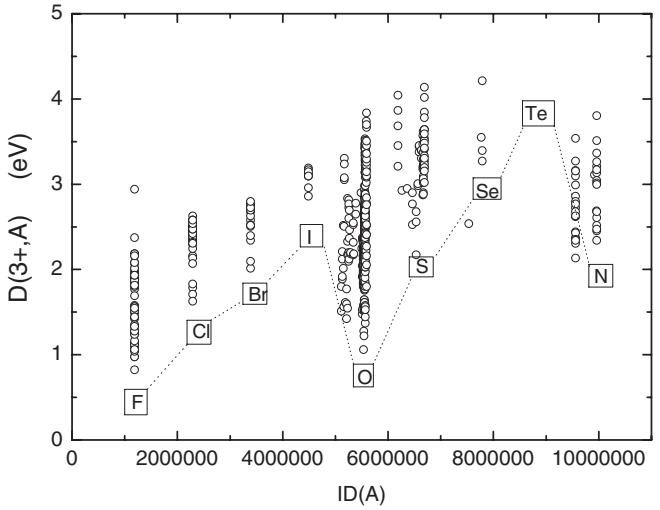

Figure 6. The redshift in trivalent lanthanides in 680 different compounds.

improved data became available and column 4 of Table I compiles the latest values on the spin allowed 4f-5d transition energy.[11]

Redshift values pertaining to about 300 different compounds were collected in[7]. More information has been collected since and Fig. 6 compiles data on $D(3+, A)$ for 680 different compounds and sites arranged following the 7-digit compound identification number. The data set shows that $D(3+, A)$ tends to increase according to the nephelauxetic sequence[12]

$$F^- < O^{2-} < Cl^- < N^{3-} \approx Br^- < I^- < S^{2-} < Se^{2-}. \qquad [4]$$

It also shows that the spread in $D(3+, A)$ is largest for the small anions F^- and O^{2-} and tends to decrease with anion size. The relationship between $D(3+, A)$ and structure and composition can be further revealed by zooming in on the data of Fig. 6 as was done in[9] for the fluorides, in[13] for the other halides, in[14] for sulfates, carbonates, phosphates, borates, and silicates, and in[15] for the aluminates and other oxides. Figure 7 shows an expanded part from the oxide data of Fig. 6. Data are now grouped following decreasing electronegativity of the most electronegative cation in the compounds

$$P^{5+} > H^+ > B^{3+} > Si^{4+} > Al^{3+} > RE^{3+} > AE^{2+} \qquad [5]$$

where RE=Rare Earth and AE=Alkaline Earth. One may observe a tending increase of redshift with smaller value for the electronegativity. By further zooming in on the data eventually relationships with changing size of the site occupied by Ce^{3+} will start to emerge.

The information on the redshift $D(3+, A)$ and the $E_{fd}(n, 3+, \text{free})$ parameters in Table I, can be combined with the Dieke diagram to construct level schemes as in Fig. 8. It shows the location of the lowest $5d_1$-levels relative to the $4f^n$ levels. A characteristic double zigzag curve is observed in the energy of the 4f-5d transition. The upper zigzag curve represents the 5d energies for the gaseous trivalent lanthanides. For the lanthanides in compound A one may simply shift the entire zigzag curve by the redshift $D(3+, A)$. In Fig. 8 a redshift of 3.41 eV was used that applies to $Y_3Al_5O_{12}$ but it can equally well be done for all 680 compounds of Fig. 6. The method has been used successfully to select potential compounds that show Pr^{3+} photon cascade emission (or quantum cutting).[16] $E_{fd_1}(2, 3+, A)$ should then be larger than the energy of 5.6 eV of the $^1S_0$ level of Pr^{3+}. Allowing for 0.4 eV Stokes shift this translates to $D(3+, A) < 1.4$ eV. Figure 6 and Fig. 7 immediately shows that only within some fluoride, phosphate, and few aluminate compounds such condition is fulfilled.

The shift model.—The observation that the redshift $D(3+, A)$ is the same for all 14 trivalent lanthanides implies that the crystal field splitting and the centroid shift must, in first approximation, be the same too. In practice this is best tested by comparing the 4f-5d transitions in

Table I. The energy of the first spin allowed 4f-5d transition in (quasi)-free Ln^{2+} and Ln^{3+} ions. For $n > 7$ the energy difference between the [HS] and [LS] $5d_1$ levels of Ln^{3+} typical for fluoride compounds is given in column 5.

n	Ln	$E_{fd}(n+1, 2+)$	$E^{sa}_{fd}(n, 3+)$	$E^{exch}(n, 3+, F)$
0	La	−0.94	–	
1	Ce	−0.35	6.12	
2	Pr	1.56	7.63	
3	Nd	1.93	8.92	
4	Pm	1.96	9.24	
5	Sm	3	9.34	
6	Eu	4.22	10.5	
7	Gd	−0.2	11.8	
8	Tb	1.19	7.78	1.0
9	Dy	2.17	9.25	0.74
10	Ho	2.25	10.1	0.51
11	Er	2.12	9.86	0.35
12	Tm	2.95	9.75	0.28
13	Yb	4.22	10.89	0.22
14	Lu		12.26	0.15

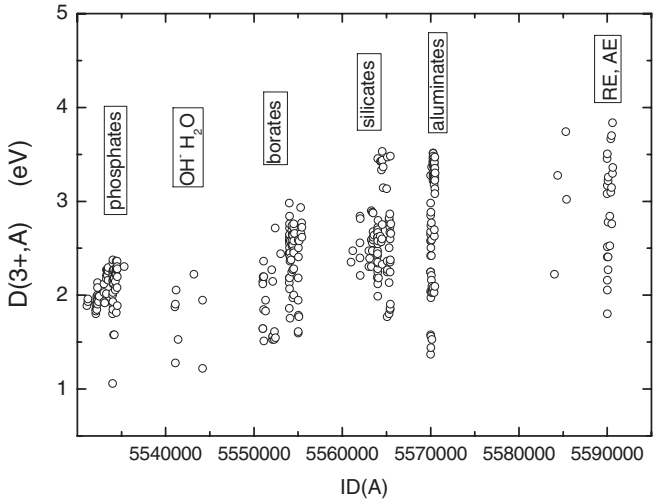

Figure 7. The redshift for trivalent lanthanides in 355 different oxide compounds.

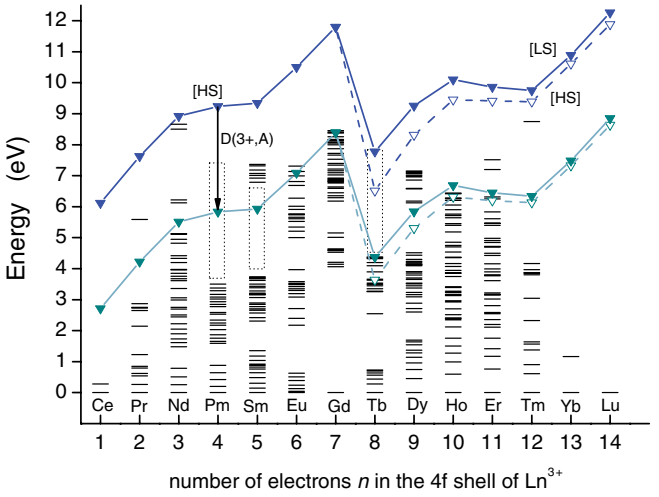

Figure 8. The 5d-levels within the Dieke diagram for the free trivalent lanthanides with $E^{exch}(8, 3+, \text{free})$ =1.27 eV. For $Y_3Al_5O_{12}$ the redshift $D(3+, A)$=3.41 eV and $E^{exch}(8, 3+, \text{Y3Al5O12})$ =0.73 eV apply.

Ce^{3+} with those in Pr^{3+} and Tb^{3+} when on the same site in the same compound as was done in,[16,17,19] Table I and Fig. 8 show that Pr^{3+} and Tb^{3+} are lanthanides with relatively low values for $E_{fd_1}(n, 3+, \text{free})$, and the higher energy 4f-5d transitions can often be observed before the onset of the fundamental absorption of the host. Furthermore the 4f-5d excitation spectra of Pr^{3+} and Tb^{3+} are relatively simple. On excitation of an electron from a $4f^n$ ground state to the 5d-configuration, the $n-1$ electrons left behind in the 4f-shell can stay behind in the ground state but also in a $4f^{n-1}$ excited state. Pr^{3+} in the excited $[Xe]4f^15d^1$ configuration has only one 4f-electron that may occupy two different 4f-levels. Tb^{3+} has the advantage that in the excited $4f^75d$ configuration the lowest $4f^7[^8S_{7/2}]$ level is relatively stable and the next higher $4f^7[^6P_J]5d_1$ levels are about 3.5-4.0 eV higher[18] enabling to observe the $4f^8$-$4f^7[^8S_{7/2}]5d_i$ transitions as isolated bands.

Figure 9 compares the excitation spectrum for Ce^{3+} and Tb^{3+} in $LiLuSiO_4$.[17] Spectrum 1) shows clearly the first two 4f-5d excitation bands for Ce^{3+} and the third one is present as a shoulder band. The same three bands reappear for Tb^{3+} at energies that are $Sh_d = 1.69$ eV higher than for Ce^{3+}. Note that this value is practically the same as the value of 1.66 eV that can be read from column 4 of Table I. Next by shifting the three intense Tb^{3+} band positions toward lower energy by an amount $Sh_{ex} = 0.92$ eV three other bands are observed of weaker intensity. The operations by the shift parameters Sh_d and Sh_{ex} are illustrated in Fig. 9. Tb^{3+} is the first lanthanide with more than half filled 4f-shell, and on excitation of one electron to the 5d-shell the spin $\vec{s}_d$ of the 5d-electron can be oriented parallel or anti-parallel to the 7/2 total spin $\vec{S}_f$ of the $4f^7$-shell. It yields a lower energy high spin [HS] (s=8/2) and a higher energy low spin [LS] (s= 6/2) level that are separated by the exchange energy $E^{exch}(8, 3+, A)$. Since the transition from the [LS] $4f^8$ ground state of Tb^{3+} to its [HS] $4f^7[^8S_{7/2}]5d_1$ is spin-forbidden it appears as a weak band in excitation spectra. In the case of $LiLuSiO_4$ the exchange splitting appears $E^{exch}(8, 3+, A) = 0.92$ eV.

For the lanthanides other than Pr^{3+} and Tb^{3+} the number of excited $4f^{n-1}$ states possible for the $n-1$ electrons left behind in the 4f-shell becomes very large which results in very complicated $4f^{n-1}5d_i$ excitation and absorption spectra containing numerous overlapping bands. Assigning the different bands is then often a hopeless task unless supported by detailed theoretical modeling with crystal field theory.[20–22] In practice the approximate shift model works only for the lowest few 4f-5d excitation bands which is for many situation already very helpful.

The exchange splitting.—The isotropic exchange interaction between the 5*d* electron spin $\vec{s}_d$ and the total spin $\vec{S}_f$ of the $n-1$ electrons in the 4f-shell leads to an energy separation[17,23]

$$E^{exch}(n, 3+, A) = -2J_0(n, 3+, A)\vec{s}_d \cdot \vec{S}_f \qquad [6]$$

with $J_0(n, 3+, A)$ the exchange interaction strength. The estimated values for $J_0(n, 3+, \text{free})$ are shown in Fig. 10 together with $E^{exch}(n, 3+, \text{free})$ for the gaseous trivalent lanthanides. The exchange splitting is maximum for Tb^{3+} and reduces continuously toward the beginning and end of the lanthanide series.

Fig. 11 shows the energy of the first spin-forbidden [HS] and first spin-allowed [LS] 4f-5d transition of Tb^{3+} against the energy of the first 4f-5d transition in Ce^{3+}. The energies for the spin allowed transitions fall on a line of unit slope parallel to those for Ce^{3+} which demonstrates that the redshift model will work well for those transitions. However, the data for the spin forbidden transitions do not run parallel and the redshift model will fail. With smaller $E_{fd}(1, 3+, A)$ or larger redshift the exchange splitting $E^{exch}(8, 3+, A)$ reduces from values of 1.27 eV for the free Tb^{3+}, to about 1.0 eV for fluoride compounds, 0.92 eV for $LiLuSIO_4$ down to values near 0.6 to 0.7 eV in compounds with the largest redshift. The reduction appears to be related to the nephelauxetic effect[24] and has been attributed to the mixing

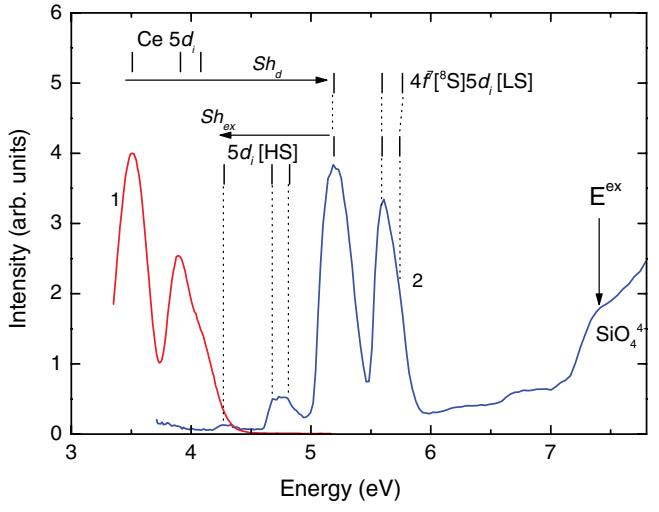

Figure 9. Excitation spectrum of 400 nm Ce^{3+} *df* emission in $LiLuSiO_4$ at 295 K (spectrum 1). Spectrum 2) excitation spectrum of 545 nm Tb^{3+} *4f-4f* emission in $LiLuSiO_4$ at 10 K. Vertical bars illustrate band positions generated by the shift model.

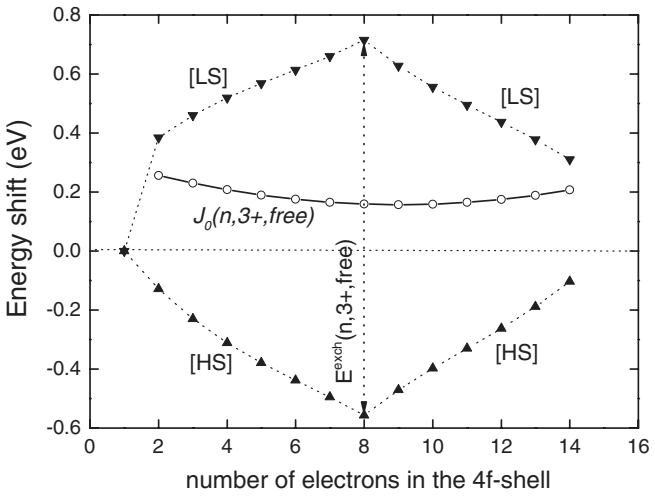

Figure 10. ◯, the exchange interaction strength $J_0(n, 3+, \text{free})$ for the trivalent free lanthanide ions. ▽, the energy shift of the low spin states and △ the energy shift of the high spin states due to the exchange interaction.

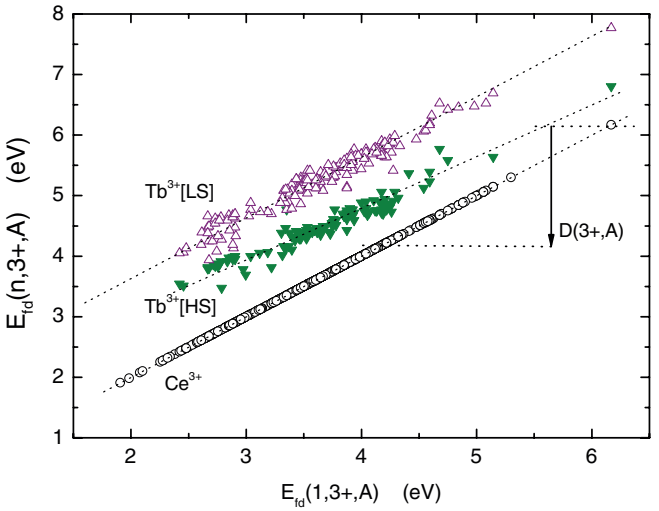

Figure 11. The energy of the first spin allowed and first spin forbidden transition in Tb^{3+} against the first 4f-5d transition energy in Ce^{3+}.

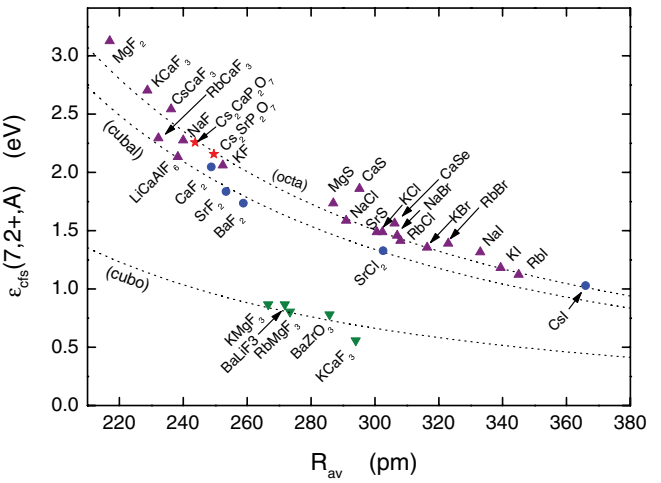

Figure 12. The crystal field splitting of the $4f^6 5d$ configuration of Eu^{2+} at sites of O_h point symmetry against the average distance to the relaxed first anion coordination shell. Data are from[28] complemented with two data points from.[29]

of the 5d-orbital with anion ligand orbitals which reduces the spin purity of the 5d-electron. Column 5 of Table I compiles $E^{exch}(n, 3+, \mathrm{F})$ that was found experimentally for the lanthanides in fluoride compounds. Then in diagrams as in Fig. 8 one may apply $D(3+, A)$ to the first spin allowed 4f-$5d_1$ transition for each lanthanide as expressed with Eq. (3). To place the energy levels of the first $4f^{n-1}5d_1$ [HS] state for $n > 7$ one may use

$$E^{s.f.}_{fd}(n, 3+, A) = E^{s.a.}_{fd}(n, 3+, A) - E^{exch}(n, 3+, \mathrm{F}) \times \mathrm{E^{exch}}(8, 3+, \mathrm{A}) \quad [7]$$

where $E^{exch}(8, 3+, A)$ needs to be obtained from experiment.

The systematics in 4f-5d transitions with type of compound.— The redshift model applies so well because the nature of the 5d-orbital is apart from the gradual lanthanide contraction about the same for all 14 lanthanides. This implies that also the interaction between the 5d electron and the chemical environment is similar leading to similar centroid shift, similar crystal field splitting, and similar Stokes shift.[10] Ce^{3+} has been very widely studied and from collecting data on 4f-5d transitions all five 4f-$5d_i$ energies are known today for Ce^{3+} in about 140 different compounds. From this data the total crystal field splitting and the centroid shift were obtained, and relationships with structure and composition were studied. This was systematically done in a series of papers[9,13–15,25,26] where it was found that the crystal field splitting is almost entirely determined by the shape and the size of the first anion coordination polyhedron around Ce^{3+}. It appears almost independent on the type of anions and the bonding with Ce^{3+}. On the other hand the centroid shift appears independent on the shape and symmetry of the coordination polyhedron; it is entirely determined by the chemical properties of the surrounding ligands.

The crystal field splitting.—By selecting compounds with the same shape of coordination polyhedron around Ce^{3+} the relationship between $\epsilon_{cfs}(1, 3+, A)$ and the size of the polyhedron can be studied. In the case of 6-fold octahedral coordination with O_h point symmetry, the crystal field interaction creates a higher energy doublet e_g and lower energy triplet t_{2g} level splitting. The ordering is reversed for 8-fold cubal and 12-fold cuboctahedral coordination.[27] This is all best illustrated for the crystal field splitting observed for Eu^{2+} as shown in Fig. 12, see.[28] Here R_{av} is defined as

$$R_{av} = \frac{1}{N}\sum_{i=1}^{N}(R_i - 0.6\Delta R) \quad [8]$$

where R_i are the individual bond lengths to the N coordinating anions in the unrelaxed lattice. $\Delta R \equiv R_M - R_{Ln}$ with R_M the ionic radius of the cation that is replaced by the lanthanide Ln with ionic radius R_{Ln}, and $0.6\Delta R$ is the estimated amount of bond length relaxation. Crystal field splitting appears to behave as

$$\epsilon_{\mathrm{cfs}} = \beta^{Q}_{\mathrm{poly}} R_{av}^{-2} \quad [9]$$

where $\beta^{Q}_{\mathrm{poly}}$ is a constant that depends on the type of coordination polyhedron and whether the lanthanide is trivalent ($Q = 3+$) or divalent ($Q = 2+$). The curves through the data in Fig. 12 are all given by Eq. (9) with $\beta_{\mathrm{octa}} = 1.36{\cdot}10^5$ eV pm^2 and $\beta^{Q}_{\mathrm{octa}}$:$\beta^{Q}_{\mathrm{cubal}}$:$\beta^{Q}_{\mathrm{cubo}}$ equals 1 to 0.89 to 0.44.[25] Data and figures like for Eu^{2+} were also published for Ce^{3+} with the same coordination polyhedra and also for coordination polyhedra like a 9-fold tri-capped trigonal prism or an 8-fold dodecahedron.[13–15,25] It is evident from graphs like Fig. 12 that higher coordination number tends to reduce the crystal field splitting. Since also the bond lengths to the surrounding anions increase with coordination number, the reduction of ϵ_{cfs} with coordination number becomes even stronger. For example the crystal field splitting for Eu^{2+} on the 6-fold octahedral Ca-site in $KCaF_3$ is 2.7 eV whereas it is 0.56 eV on the 12-fold cuboctahedral K-site in the same compound. Figure 12 also clearly reveals that the type of anion, whether it is F, S, Cl, Se, I, or Br seems not to matter at all. This was recently also confirmed for oxide compounds by Srivastava et al.[29] Eu^{2+} occupies octahedral sites in $Cs_2CaP_2O_7$ and $Cs_2SrP_2O_7$ and the crystal field splitting agrees excellently with Eq. (9) as demonstrated by the two star data symbols in Fig. 12.

The large variation in the crystal field splitting explains partly the appearance of the data in Fig. 6. The maximum size of the crystal field splitting and then also the variation from compound to compound is largest for the smallest anions F^- and O^{2-} which leads to a wide spread in redshift values. When the anion gets larger from F to Cl, Br, I or from O to S, Se, the crystal field splitting tends to decreases for two reasons. R_{av} increases but also the spread in coordination number for large anions is smaller; 12-fold coordination with iodine or sulfur does not occur.

From comparing Eu^{2+} ϵ_{cfs} data with Ce^{3+} data it follows that $\beta^{2+}_{\mathrm{poly}} = 0.81\ \beta^{3+}_{\mathrm{poly}}$. If one also takes the 12 pm larger size of Eu^{2+} into account, Eq. (9) yields $\epsilon_{\mathrm{cfs}}(7, 2+, A) \approx 0.77\epsilon_{\mathrm{cfs}}(1, 3+, A)$.[28]

Crystal field splitting is caused by the exchange, Pauling, and coulomb interaction between the 5*d* electron and anion ligands. Suppose Ce^{3+} is replaced by the smaller Tb^{3+} ion and lattice relaxation does not occur. The interactions become less strong and crystal field splitting decreases. Although lattice relaxation partly cancels this effect, smaller crystal field splitting is still expected for Tb^{3+}. For CaF_2,

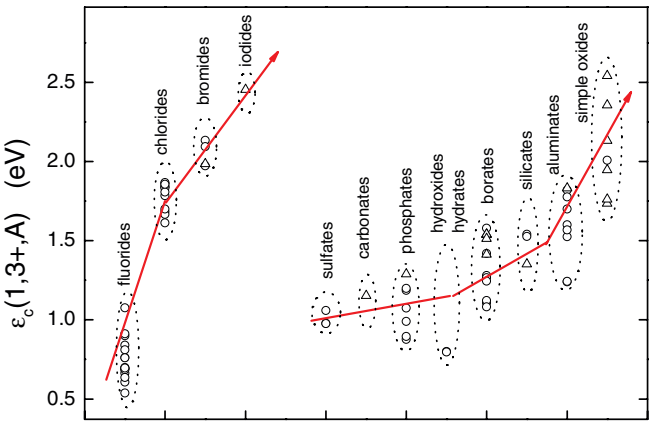

Figure 13. The centroid shift for the Ce^{3+} 5d-configuration in halides and oxide compounds.

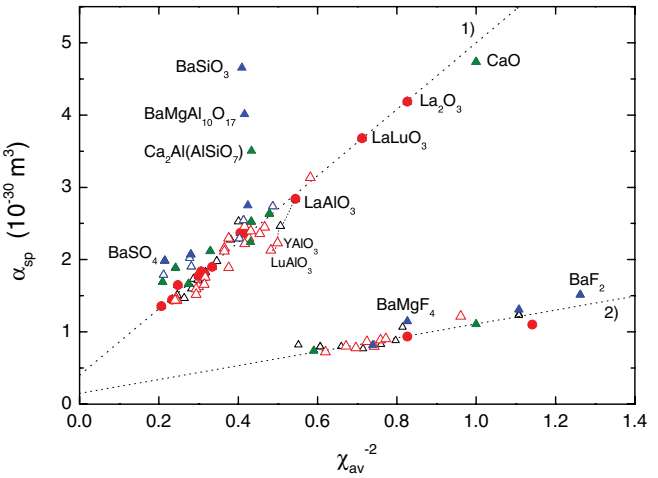

Figure 14. The spectroscopic polarizability as derived from the observed centroid shift in oxide and fluoride compounds. Solid data symbols pertain to Ce on La-sites and open data symbols (in red) to Y or Lu sites and (in blue) to Sr and Ba sites. The parameters for the dashed line 1) are $\alpha_0(O)$ =0.4, $b(O)$ =4.6, and for line 2) are $\alpha_0(F)$ =0.15 and $b(F)$ =0.96.

YPO_4, and $LiYF_4$ van Pieterson et al.[30,31] found that the 5*d* crystal field splitting of Tb^{3+} is 5% smaller than that of Ce^{3+}. A 9% decrease was observed for the even smaller lanthanides Tm^{3+} and Yb^{3+}. In[17] it was found that the size of the deviations between the redshift for Ce^{3+} and Tb^{3+} scales with the size of the ϵ_{cfs}. Such variations in the crystal field splitting will translate to variations in the redshift and limits the accuracy of the redshift model. Part of the deviations from the straight unit slope lines in Fig. 11 are caused by this.

The centroid shift.—Figure 13 shows the centroid shift $\epsilon(1, 3+, A)$ for Ce^{3+} as was found in fluorides, chlorides, bromides, and iodides. For the oxide compounds a sub-grouping that follows decreasing electronegativity of the most electronegative cation (S, C, P, H, B, S, Al, RE+AE) was made. One clearly observes the trends of increase of centroid shift that follows the nephelauxetic series of Eq. (4) and Eq. (5), and evidently the centroid shift is the basis for the increase in redshift value observed in Fig. 7 along the series of Eq. (5).

When in quantum mechanics all five 5d-wave functions are added one obtains a spherical symmetric wave function with spherical symmetric 5d-charge distribution. The centroid shift is then due to the interaction of such distribution with its chemical environment, and one may imagine that it will be independent on the shape or symmetry of the coordination polyhedron. This is indeed what is observed experimentally.

According to Morrison[32] the centroid shift in fluoride compounds is due to the correlated motion of the 5d-electron and the electrons in the surrounding ligands. In oxides and other compounds also the covalence (charge sharing) between the 5d-orbital and the ligand orbitals is important.[6,33] The contribution ϵ_2 from the correlated motion can be calculated classically, and in first order approximation one obtains[32]

$$\epsilon_2 = \frac{e^2}{4\pi\epsilon_0}(< r^2 >_{5d} - < r^2 >_{4f}) \sum_{i=1}^{N} \frac{\alpha_i}{(R_i - 0.6\Delta R)^6} \qquad [10]$$

where r represents the position of the electron in either the 5*d* or 4*f* orbital, and $< r^2 >$ is the expectation value of r^2. α_i is the polarizability of ligand i located a distance R_i from Ce^{3+} in the unrelaxed lattice. The summation is over all N coordinating anion ligands. Assuming that the contribution ϵ_1 from the covalence is proportional to ϵ_2 and that all ligands are equivalent, one may replace α_i with an effective polarizability, that was named the spectroscopic polarizability α_{sp}, to obtain[9,26]

$$\epsilon_c = \epsilon_1 + \epsilon_2 = 1.79 \times 10^{13} \alpha_{sp} \sum_{i=1}^{N} \frac{1}{(R_i - 0.6\Delta R)^6} \qquad [11]$$

where R_i is in pm, energy in eV, and α_{sp} in 10^{-30} m^3. α_{sp} characterizes the chemical property of the anion ligand which is determined by the type of anion (F, Cl, Br, I, O, S, Se, Te, N) but also by the cations that bind the anion ligands. One may relate the average bonding strength of the ligand electrons to the average electronegativity χ_{av} of the cations in the compound defined as

$$\chi_{av} = \frac{\sum_i n_i z_i \chi_i}{\sum_i n_i z_i} \qquad [12]$$

where n_i is the number of cations of type i with charge $+z_i$ and electronegativity χ_i in the compound formula. With Pauling type[34] electronegativity values χ_i, that were corrected and compiled by Allred,[35] χ_{av} can be easily determined for each compound. For example, $\chi_{av}(CaSO_4) = (2\chi_{Ca} + 6\chi_S)/8 = 2.19$. Then by using arguments borrowed from theory on the force constant of metal-hydride bonds in diatomic molecules the following linear relationship was proposed[26]

$$\alpha_{sp} = \alpha_0(X) + \frac{b(X)}{\chi_{av}^2} \qquad [13]$$

where $\alpha_0(X)$ is the limiting spectroscopic polarizability of anion X in the case of very large χ_{av}, i.e., in the case of strong binding of the anion valence electrons to cations. One may interpret $b(X)$ as the susceptibility of anion X to change its polarizability due to its bonding with coordinating cations.

Figure 14 shows the α_{sp}, as derived from the structure and composition of the compound and the observed centroid shift, against the inverse square of the average electronegativity. Clear linear relationships emerge. There are few strongly deviating points but these concern compounds with Ba-sites with very large ΔR, and since Eq. (10) is quite sensitive to the bond lengths any deviation from the assumed $0.6\Delta R$ relaxation will affect strongly the obtained α_{sp}. For Ce^{3+} on a rare earth La, Gd, Y, Lu) site data follow quite well Eq. (13). This enables to predict the centroid shift from the composition and structure of the compound. It even predicts well the centroid shift for the mixed anion compound $La_3F_3[Si_3O_9]$.[36]

The centroid shift, the spectroscopic polarizability, the average cation electronegativity are all strongly tied to the nephelauxetic sequence. Actually, one may regard $\epsilon_c(1, 3+, A)$ and perhaps even more α_{sp} as a quantification of the nephelauxetic effect. Inspecting again Fig. 6 one observes that the redshift tends to increase along with the nephelauxetic sequence which can now entirely be attributed to the centroid shift.

Fig. 15 shows the exchange splitting $E^{exch}(8, 3+, A)$ against the compound classification number. Like for the redshift and the centroid shift a correlation with the nephelauxetic sequence can be observed.

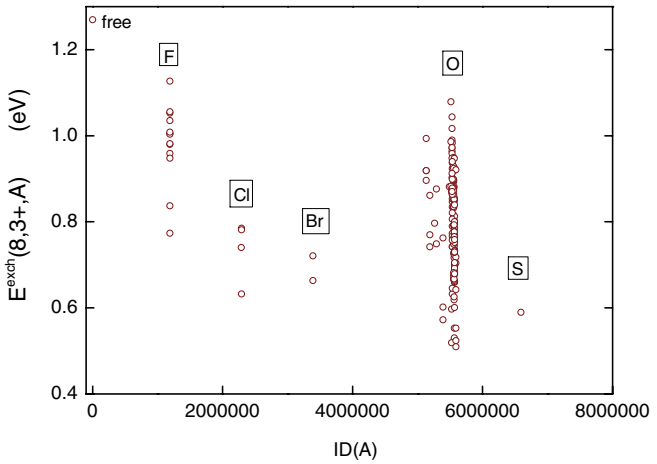

Figure 15. Exchange splitting $E^{exch}(8, 3+, A)$ against the compound classification number.

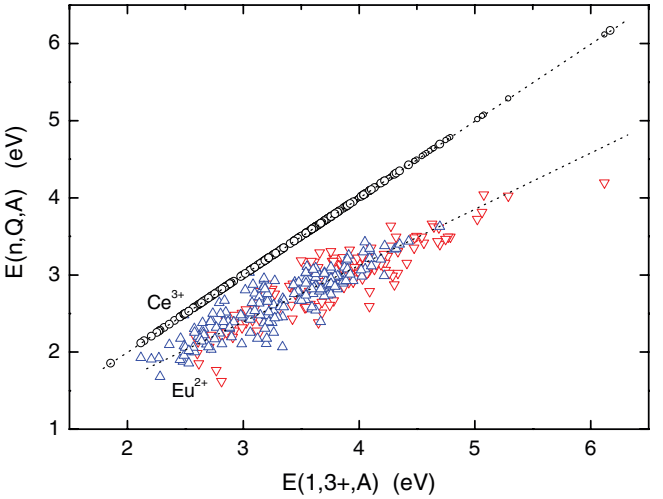

Figure 16. The energy of the 4f-5d transition in Eu against that in Ce. △ is data based on emission and ▽ is data based on absorption.

Along that sequence the polarizability of the anion ligands and the covalence (charge sharing) between the 5d-orbital and the anion ligands increases. This goes at the expense of the interaction between the 5d spin and total 4f-electron spin, and the exchange splitting decreases.[17]

The divalent lanthanides.— The story for the divalent lanthanides is analogous as for the trivalent ones. Unlike for Ce^{3+} with only one electron in the 4f-shell where plenty of data is available on, there is no information on La^{2+} also with one electron in 4f. La^{2+} is never a stable impurity in compounds. Only for Eu^{2+}, Yb^{2+}, Sm^{2+}, and Tm^{2+} sufficient amount of data is available to test the redshift model. Again it applies very well and one may define analogously the lanthanide independent redshift $D(2+, A)$ for divalent lanthanides.[37] By far most data is available on Eu^{2+} doped compounds that then forms a bases to determine the value for the redshift. A compilation involving about 300 different compounds was published in[8] and similar figures as in Fig. 6 and Fig. 7 were presented. In the 4f-5d excitation spectra of Eu^{2+} always about 0.8 eV wide bands appear because the 6 electrons remaining in the 4f-shell may occupy one of the seven ^7F_J states that spread about 0.6 eV in energy. To properly determine the redshift one should determine the energy of the transition to the $4f^6[^7F_0]5d_1$ level where the six electrons remain in the ground $4f^6$ state. Ideally all seven transitions can be seen individually and the excitation or absorption spectrum shows a characteristic staircase structure.[38,39] However, usually everything is smeared out into a featureless 1 eV broad band that often overlaps with the transitions to $4f^65d_2$ and higher $4f^65d_i$ states. In those cases the first 4f-5d excitation is estimated at the energy where the excitation spectrum has increased to about 15-20% of the maximum of the first ≈0.8 eV wide $4f^6[^7F_J]$ excitation band.[8] In other work occasionally the intercept between the normalized excitation and normalized emission band is taken. Figure 16 shows $E_{fd}(6, 2+, A)$ against $E_{fd}(1, 3+, A)$. It demonstrates a correlation between both. When data are analyzed in terms of the redshift a roughly linear relationship between the redshift $D(3+, A)$ and $D(2+, A)$ is obtained

$$D(2+, A) = 0.64D(3+, A) - 0.233\,\text{eV} \qquad [14]$$

which implies that the first 4f-5d absorption energy of Eu^{2+} and therewith for all divalent lanthanides can be estimated from the redshift for Ce^{3+} and vice versa with about ±0.15 eV standard deviation. The wealth of data on trivalent lanthanides can then be related with the wealth of data on divalent lanthanides.

The Charge Transfer Bands and HRBE Schemes

The transitions of type 3 in Fig. 2 between a lanthanide state and a host band state provide information on the location of the lanthanide state with respect to either the valence band or the conduction band. The excitation of an electron from the valence band to the 4f-shell of a trivalent lanthanide creates the divalent lanthanide plus a hole on the neighboring anion ligand. This transition appears as a typically 0.8 eV broad band in absorption and luminescence excitation spectra of the trivalent lanthanides. The energy of this band shows very characteristic and systematic change with the number of electrons n in the 4f-shell. Data on the CT-band energy have been collected for the trivalent lanthanides in many different compounds.[40,41] Most information is available on Eu^{3+} followed by Yb^{3+}, Sm^{3+}, and Tm^{3+}. The data are shown in Fig. 17 against the CT-band energy for Eu^{3+}.

One observes, just like for the 4f-5d transition energies, that the CT-band energy to a trivalent lanthanide is always a fixed amount of energy larger than to Eu^{3+} when in the same site of the same compound. For the other trivalent lanthanides, CT-data is more scarce and often only information is available for few fluoride compounds. However also for those data fixed energy differences appear. The average energy differences

$$\Delta E(n+1, 7, 2+) \equiv \overline{E^{CT}(n, 3+, A) - E^{CT}(6, 3+, A)} \qquad [15]$$

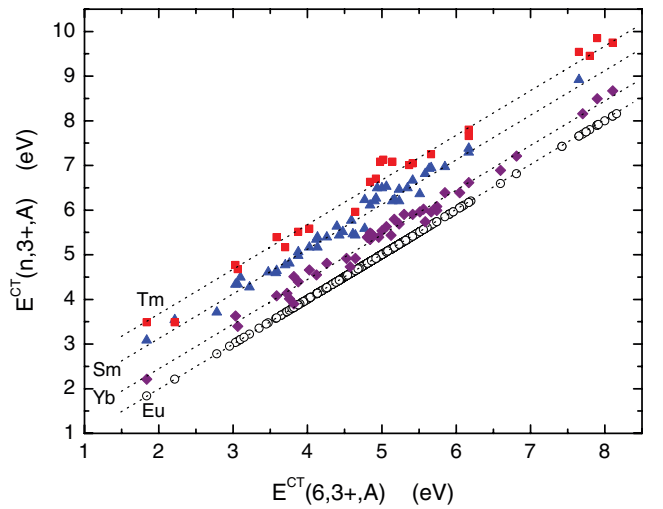

Figure 17. The energy of electron transfer bands in Eu^{3+}, Yb^{3+}, Sm^{3+} and Tm^{3+} doped compounds.

Table II. Parameter values (in eV) that define the 4f-electron binding energy zigzag curves for the divalent and trivalent lanthanides in compounds.

n	Ln	$\Delta E(n+1,7,2+)$	$\Delta E(n,6,3+)$
0	La	5.61	–
1	Ce	4.13	5.24
2	Pr	2.87	3.39
3	Nd	2.43	1.9
4	Pm	2.34	1.46
5	Sm	1.25	1.27
6	Eu	0	0
7	Gd	4.56	– 1.34
8	Tb	3.21	3.57
9	Dy	2.27	2.15
10	Ho	2.4	1.05
11	Er	2.58	1.12
12	Tm	1.72	1.28
13	Yb	0.433	0.236
14	Lu	–	

are compiled in Table II. With the knowledge that $\Delta E(n+1,7,2+)$ are independent on type of compound one obtains

$$E^{CT}(n,3+,A) = E^{CT}(6,3+,A) + \Delta E(n+1,7,2+) \qquad [16]$$

as a tool to predict the energy of all CT-bands.

$E^{CT}(6,3+,A)$ values can be obtained from experimentally observed Eu^{3+} CT-band energies or derived from CT-band energies observed for other lanthanides. For example Eu in a sulfide or nitride compound is often hard or impossible to stabilize as trivalent impurity. In that case the energy of CT can be derived from the more stable Yb^{3+} or even more stable Sm^{3+} dopant. Figure 18 gives an overview on $E^{CT}(6,3+,A)$ data in 540 different compounds mined from the archival literature. CT-energies tend to reduce in the sequence F, O, Cl, Br, S, I, N, Se, and like for the centroid shift and exchange splitting, one observes a correlation with the nephelauxetic series of Eq. (4).

The electron transfer is regarded a localized transition from a neighboring anion ligand to the 4f-shell of Ln^{3+}. The initial state is then that of an electron at the top of the valence band where the density of states is large (the Γ-point in k-space), and the final state is when the electron is in the ground state of the $4f^{n+1}$ configuration. The energy of the transition then in first approximation provides the location of the 4f ground state level above the top of the valence band. However,

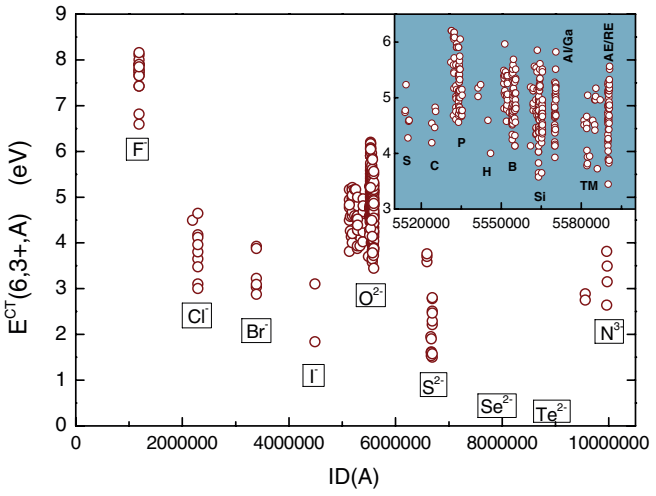

Figure 18. The energy $E^{CT}(6,3+,A)$ of electron transfer from the valence band to Eu^{3+} in 540 different compounds. The inset is an expanded view of the data on oxide compounds where data are grouped in sulfates (S), carbonates (C), phosphates (P) etc. (TM is a transition metal, AE is an alkaline earth, and RE is a rare earth cation).

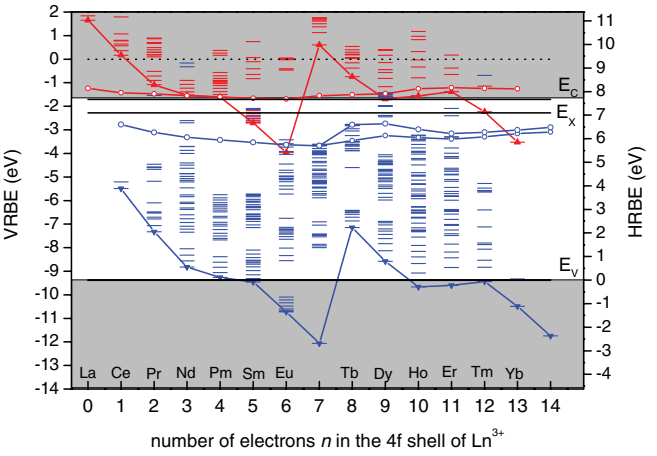

Figure 19. The HRBE and VRBE of the divalent and trivalent lanthanides in $Y_3Al_5O_{12}$.

after the transition the lattice is out of equilibrium and relaxation will take place affecting the ground state energy location. Yet, it turns out that the energy of CT still provides a good measure for the location of the divalent lanthanide 4f-ground state above the top of the valence band. This was attributed to a cancellation effect;[40] the energy gained in lattice relaxation cancels against the energy required to remove the hole on the neighboring anion.

The correspondence between CT-energy and location of the divalent ground state above the valence band was independently confirmed by thermoluminescence studies on double lanthanide doped YPO_4:Ce^{3+};Ln^{3+} phosphors.[42,43] These studies complemented with information from other sources eventually led to the set of $\Delta E(n+1,7,2+)$ values in Table II.[11] One only needs the value for $E^{CT}(6,3+,A)$ to place all ground state levels of the divalent lanthanides above the valence band. Figure 19 shows the location of the divalent ground state energies for $Y_3Al_5O_{12}$. They follow a characteristic double zigzag curve pattern. A similar curve applies to the ground state energy for the trivalent lanthanides. The values for $\Delta E(n,6,3)$ that define the trivalent zigzag curve are compiled in column 4 of Table II. They were established by combining data from different types of experiments, and the reader is referred to[11] for further information. One only needs to pin the trivalent zigzag curve relative to the conduction band bottom which can be done with photoconductivity studies on Ce^{3+} doped compounds or by studying the thermal quenching of 5d-4f luminescence. Here, the energy at the bottom of the conduction band may proof difficult to establish. As rule of thumb it is usually taken equal to $1.08\times E^{ex}(A)$ where $E^{ex}(A)$ is the energy needed to create a host exciton state and the factor of 1.08 accounts for the electron-hole binding energy of the exciton. Note that the thus defined mobility band edge energy is significantly larger (≈15%) than the fundamental optical abosorption band edge energy. Once the $4f^n$ ground state energies are known also the excited $4f^n$ states and excited $4f^{n-1}5d$ states can be placed in the scheme by using the Dieke diagram and the redshift models. Note that the collection of the Ln^{3+} levels in the HRBE scheme is almost an inverted version of Fig. 8. The location of the lowest 5d-state is relatively constant with the number of electrons in the 4f-shell. This is related to the fact that the nature of the 5d-orbital for all lanthanides is quite the same; then the interaction with the chemical environment is similar too leading to similar 5d-energy. The 5d-electron energy in the divalent lanthanide is always higher than that in the trivalent one simply because of the smaller coulomb attraction by the less positive ion core. The energy difference depends on type of compound and is usually 1.0± 0.5 eV. Note that in Fig. 19 the 5d-level for the divalent lanthanides is close to the bottom of the conduction band. This is not a coincidence but to be expected for a divalent lanthanide on a trivalent rare earth site. The localized 5d-electron in Eu^{2+} is bonded by the Eu^{3+}

core ion quite similar to an itinerant electron at the bottom of the conduction band that is bonded by the RE^{3+} ions of the host compound.[44]

HRBE schemes as in Fig. 19 were published for many compounds. They provide the coulomb correlation energy $U(6, A)$ defined as

$$U(6, A) \equiv E_{4f}(7, 2+, A) - E_{4f}(6, 3+, A) \quad [17]$$

which is the energy difference between the ground state energy of Eu^{2+} and that of Eu^{3+}. In fluorides $U(6, A)$ is found between 7.65 and 7.3 eV, in oxides it ranges from 7.2 to 6.4 eV. Chlorides and bromides range from 6.8 to 6.6 eV, for compounds with the large polarizable iodide anions $U(6, A)$ is about 6.3 eV, and for sulfides and selenides it reduces to ≈6.2 eV.[45] Again the nephelauxetic sequence of Eq. (4) is followed.

The Chemical Shift Model and VRBE Schemes

Recently a new chapter was added to the systematics in the lanthanide level energies.[46] In the redshift and centroid shift models, the lanthanide level energies, particularly those of $5d_1$, relative to the $4f^n$ ground state were the topic. Those models were followed by models on charge transfer energies and methods to place the lanthanide levels relative to the valence band. The models combined provide the HRBE-schemes with all lanthanide level locations relative to the host bands. The latest model relates all lanthanide levels plus the host bands to the vacuum energy $E_{vac} \equiv 0$, i.e., it relates the binding energy of an electron in the host band or a lanthanide impurity state to the energy of an electron at rest in vacuum.

Figure 20 shows the experimental absolute binding energy of electrons in the 4f-shell of the divalent and trivalent lanthanides when in vacuum, when surrounded by water, and when surrounded by the free conduction band electrons of the pure lanthanide metals.[46] The binding energy $E_{4f}(7, 2+, \text{vacuum}) = -24.92$ eV for an electron in the 4f-shell of the free ion Eu^{2+} is weakened to −4.0 eV when surrounded by water and even further to −3.7 eV when surrounded by free electrons in Eu-metal. The negative charge of the chemical environment around Eu^{2+} creates a repulsive coulomb interaction with the 4f-electron leading to the upward shift in binding energy. This chemical shift $E(Eu^{3+}, A)$ for Eu^{3+} is always larger than that for Eu^{2+} resulting in a reduction of $U(6, A)$ as compared to the value of 18.05 eV in vacuum, see Eq. (17).

The chemical shift model relates the size of $U(6, A)$ with the size of the chemical shift which led to

$$E_{4f}(7, 2+, A) = -24.92 + \frac{18.05 - U(6, A)}{0.777 - 0.0353U(6, A)} \quad [18]$$

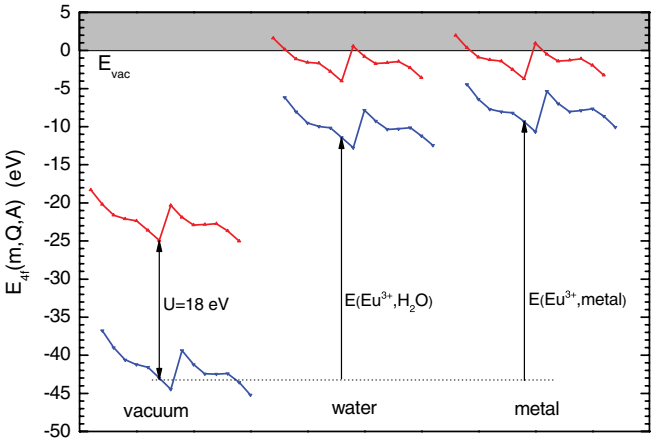

Figure 20. Scheme with the 4f-VRBE $E_{4f}(m, Q, A)$ of the divalent (Q=2+; upper curves) and trivalent (Q=3+; lower curves) lanthanide ions. The curves on the left pertain to A=vacuum, in the middle to A=H_2O, and on the right to A=metal. The size of the chemical shift $E(Eu^{3+}, A)$ are indicated by the arrows.

Knowledge on $U(6, A)$, that can be obtained from a HRBE-scheme, is then sufficient to determine the absolute 4f-electron binding energy in Eu^{2+} which then pins the entire HRBE scheme relative to E_{vac}. For $Y_3Al_5O_{12}$ in Fig. 19 with $U(6, A)$=6.75 eV, $E_{4f}(7, 2+, Y_3Al_5O_{12})$ becomes −3.95 eV and the right hand HRBE energy scale can be converted into the left hand VRBE energy scale.

The chemical shift model still needs to be tested more severely but already promising results are obtained. In constructing the double zigzag curves of 4f-electron binding energy with the parameters in Table II it is assumed that the shapes of those curves are independent on the type of compound. This started as an empirical observation but with the chemical shift model it is understood why this is the case. A closer observation of the double zigzag curves in Fig. 20 will show that the zigzag curves for water and metal are tilted versions of those for the free ions; the shape of the zigzag curve is not truly universal. The tilting can be expressed as

$$E_{4f}(n, Q, A) = E_{4f}(n, Q, \text{vacuum}) + \text{E}(\text{Eu}^{\text{Q}}, \text{A}) + \alpha(\text{Q}, \text{A})\Delta\text{R}(\text{n}) \quad [19]$$

where $E(Eu^Q, A)$ is the chemical shift of the 4f-electron binding energy in Eu with charge Q in compound A. $\Delta R(n)$ is the difference in ionic radius of the lanthanide ion with m electrons in the 4f-shell with that of the Eu ion. $\alpha(Q, A)$ was named the *contraction tilt* parameter, and it defines the tilting of the double zigzag curve around the point at $E_{4f}(7, 2+, A)$ when Q=2+ (this is Eu^{2+}) and around $E_{4f}(6, 3+, A)$ when Q=3+ (this is Eu^{3+}). The original version of Eq.(19) was proposed by Pedrini et al.,[47] and a variant was used by Thiel et al. to explain photoelectron spectroscopy (PES) data on various trivalent lanthanide doped compounds and the pure lanthanide metals.[48] Within the chemical shift model the contraction tilt parameter can be related to the square of the chemical shift as

$$\alpha(Q, A) = f\frac{E(Eu^Q, A)^2}{1440Q}[\text{eV/pm}]. \quad [20]$$

where f=0.6-0.8 expresses the fraction of $\Delta R(n)$ that the ligands relax toward the lanthanides ion. Since $7.6 < U(6, A) < 6.0$ one finds that the variation in $\alpha(Q, A)$ is marginal and one may safely use the parameters in Table II for all compounds alike. Errors made are predicted to stay within ±0.1 eV.

Latest Developments

An important outcome of the chemical shift model is that the binding energy of 4f-electrons in Eu^{2+} in the entire family of inorganic compounds appears always between −4.4 eV and −3.8 eV and it varies predictably with the nephelauxetic sequence. This is an immediate consequence of Eq. (18) and that 7.6 eV < $U(6, A)$ < 6.0 eV. It implies that the energy $E^{CT}(6, 3+, A)$ in Fig. 18 is almost entirely determined by the binding energy at the top of the valence band E_V. Figure 21 shows collected data on the host exciton creation energy $E^{ex}(A)$. With type of anion it follows a similar pattern as $E^{CT}(6, 3+, A)$ in Fig. 18.

One may now exploit the available information on $E^{CT}(6, 3+, A)$, $E^{ex}(A)$, $D(Q, A)$, and $U(6, A)$ using Eq. (18) to construct detailed VRBE schemes throughout the entire family of inorganic compounds. Figure 22 demonstrates what new insight this may provide. It shows the electron binding energy in the ground and first two excited states of Ce^{3+} together with that in the host exciton (E_X), that at the top of the valence (E_V), and that at the bottom of the conduction band (E_C) in perovskite and garnet compounds. The binding energy in the Ce^{3+} 4f-level appears surprisingly constant. The main changes are in the binding energy in the valence and conduction band and in the Ce^{3+} 5d-levels. In the rare earth perovskites $REAlO_3$, the binding energy of the $5d_1$ level is quite constant but the conduction band moves up with smaller size of the RE (La to Gd to Y to Lu). The absence of Ce^{3+} emission in $LaAlO_3$ must then be attributed to the low lying conduction band and the high lying conduction band in $LuAlO_3$ provides a high thermal stability of the Ce^{3+} 5d-4f emission.

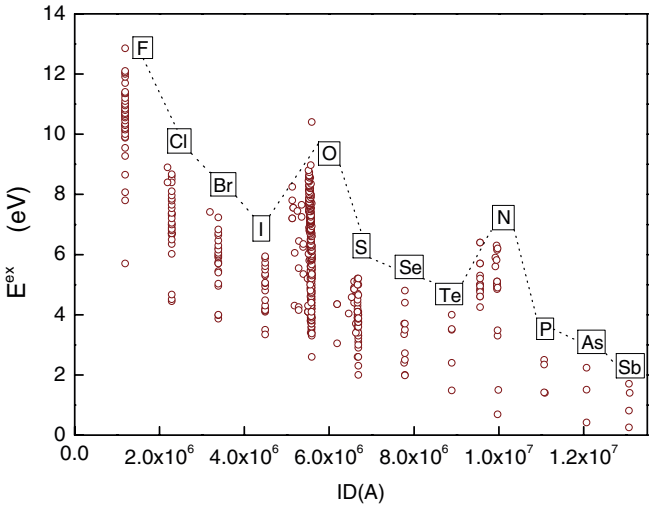

Figure 21. The host exciton creation energy $E^{ex}(A)$ in about 700 different compounds at temperature near 10 K.

In the garnet compounds the $5d_1$ level is at 1 eV lower energy due to the exceptionally large crystal field splitting. However also the conduction band is at significant lower energy. Few 0.1 eV change in either the $5d_i$ energy or the conduction band energy when the host RE changes (Gd, Y, Lu) or when Al is replaced by Ga can have important consequence for the luminescence properties.[49,50]

Final Remarks and Outlook

This work has reviewed a continuous effort during past 15 years to collect data on lanthanide spectroscopy, to analyze it, to identify trends with changing type of lanthanide and changing type of compound, and finally to arrive at models and predictive tools. It has led to the redshift, centroid shift, crystal field splitting, and exchange splitting models that predict lanthanide 4f-5d transitions. The charge transfer model predicts the energy for electron transfer from the valence band to the 4f-shell and this forms the basis to construct the host referred binding energy schemes (HRBE). The latest model is about the chemical shift of the 4f-electron binding energy of lanthanide impurities and it pins an entire HRBE scheme relative to the energy of an electron at rest in vacuum.

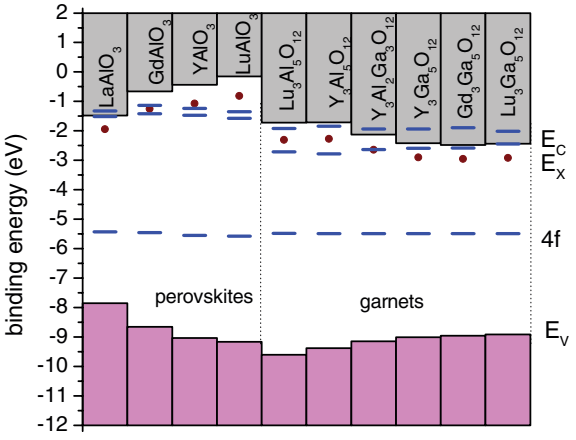

Figure 22. Vacuum referred binding energies of electrons at the top of the valence band (E_V) and the bottom of the conduction band (E_C) in several rare earth perovskite and garnet compounds. Horizontal bars indicate the VRBE of electrons in the 4f ground state and, at higher energy, the first two 5d excited states of Ce^{3+} impurities. The solid symbol denotes the electron binding energy in the host exciton state.

By means of diagrams as in Fig. 22 one may for the first time systematically study how structure, composition, and chemistry of compounds interrelate, and how that all affects lanthanide level location and optical properties. Lanthanide spectroscopy combined with the various presented models provide a new tool to obtain electron binding energies at the top of the valence band, i.e., the work function, and at the bottom of the conduction band, i.e., the electron affinity which is of interest to other fields of science. Now that methods to generate 4f-VRBE schemes for lanthanide doped compounds are available, a new challenge arises. Can we develop similar models and methods to determine the VRBE of actinides with partly filled 5f-shells, transition metal elements with partly filled d-shells, and Tl^+, Pb^{2+}, and Bi^{3+} with a filled outer $6s^2$-shell? It is extremely interesting to have knowledge on where to expect the VRBEs of electrons in transition metal or $6s^2$ impurity states with respect to that in the lanthanide states. One may then understand and predict properties of compounds activated with for example a lanthanide together with a transition metal element; a functional materials research field that is still largely unexplored.

References

1. P. Dorenbos, T. Shalapska, G. Stryganyuk, A. Gektin, and A. Voloshinovskii, *J. Lumin.*, **131**, 633 (2011).
2. R. D. Shannon, *Acta Crystallogr. Sect. A: Cryst. Phys., Diffr., Theor. Gen. Crystallogr.*, **32**, 751 (1976).
3. G. H. Dieke and H. M. Crosswhite, *Applied Optics*, **2**, 675 (1963).
4. R. T. Wegh, A. Meijerink, R.-J. Lamminmäki, and J. Hölsä, *J. Lumin.*, **87-89**, 1002 (2000).
5. P. S. Peijzel, A. Meijerink, R. T. Wegh, M. F. Reid, and G. W. Burdick, *J. Solid State Chem.*, **178**, 448 (2005).
6. J. Andriessen, P. Dorenbos, and C. W. E. van Eijk, *Phys. Rev. B*, **72**, 045129 (2005).
7. P. Dorenbos, *J. Lumin.*, **91**, 155 (2000).
8. P. Dorenbos, *J. Lumin.*, **104**, 239 (2003).
9. P. Dorenbos, *Phys. Rev. B*, **62**, 15640 (2000).
10. P. Dorenbos, *J. Lumin.*, **91**, 91 (2000).
11. P. Dorenbos, A. H. Krumpel, E. van der Kolk, P. Boutinaud, M. Bettinelli, and E. Cavalli, *Optical Materials*, **32**, 1681 (2010).
12. C. K. Jörgensen, *Absorption spectra and chemical boding in complexes*, Pergamon Press, Oxford (1962).
13. P. Dorenbos, *Phys. Rev. B*, **62**, 15650 (2000).
14. P. Dorenbos, *Phys. Rev. B*, **64**, 125117 (2001).
15. P. Dorenbos, *J. Lumin.*, **99**, 283 (2002).
16. E. van der Kolk, P. Dorenbos, A. P. Vink, R. C. Perego, C. W. E. van Eijk, and A. R. Lakshmanan, *Phys. Rev. B*, **64**, 195129 (2001).
17. P. Dorenbos, *J. Phys.: Condens. Matter*, **15**, 6249 (2003).
18. L. van Pieterson, M. F. Reid, and A. Meijerink, *Phys. Rev. Lett.*, **88**, 067405 (2002).
19. N. L. J. Le Masson, A. P. Vink, P. Dorenbos, A. J. J. Bos, C. W. E. van Eijk, and J. P. Chaminade, *J. Lumin.*, **101**, 175 (2003).
20. Chonggeng Ma, Peter A. Tanner, Shangda Xia, and Min Yin, *Optical Materials*, **29**, 1620 (2007).
21. C. G. Ma, M. G. Brik, V. Kiisk, and I. Sildos, *J. Lumin.*, in press (2012).
22. L. Ning, C. Duan, S. Xia, M. F. Reid, and P. A. Tanner, *J. All. and Comp.*, **366**, 34 (2004).
23. A. Yanase and T. Kasuya, *Progr. Theor. Phys.*, **Suppl. No. 46**, 388 (1970).
24. Jingsheng Shi and Siyuan Zhang, *J. Phys.: Condens. Matter*, **15**, 4101 (2003).
25. P. Dorenbos, *J. Alloys Compounds*, **341**, 156 (2002).
26. P. Dorenbos, *Phys. Rev. B*, **65**, 235110 (2002).
27. B. Henderson and G. F. Imbush, *Optical Spectroscopy of Inorganic Solids*, Clarendon Press, Oxford (1989).
28. P. Dorenbos, *J. Phys.: Condens. Matter*, **15**, 4797 (2003).
29. A. M. Srivastava, H. A. Comanzo, S. Camardello, S. B. Chaney, M. Aycibin, and U. Happek, *J. Lumin.*, **129**, 919 (2009).
30. L. van Pieterson, M. F. Reid, R. T. Wegh, S. Soverna, and A. Meijerink, *Phys. Rev. B*, **65**, 045113 (2002).
31. L. van Pieterson, M. F. Reid, G. W. Burdick, and A. Meijerink, *Phys. Rev. B*, **65**, 045114 (2002).
32. C. A. Morrison, *J. Chem. Phys.*, **72**, 1001 (1980).
33. B. F. Aull and H. P. Jenssen, *Phys. Rev. B*, **34**, 6640 (1986).
34. L. Pauling, *The nature Of The Chemical Bond*, Cornell University Press, New York (1960).
35. A. L. Allred, *J. Inorg. Nucl. Chem.*, **17**, 215 (1961).
36. P. Dorenbos, *J. Lumin.*, **105**, 117 (2003).
37. P. Dorenbos, *J. Phys.: Condens. Matter*, **15**, 575 (2003).
38. J. O. Rubio, S. Murrieta, J. A. Hernandez, and E. P. Munoz, *Phys. Rev. B*, **24**, 4847 (1981).
39. J. Sugar and N. Spector, *J. Opt. Soc. America*, **64**, 1484 (1974).
40. P. Dorenbos, *J. Phys.: Condens. Matter*, **15**, 8417 (2003).
41. P. Dorenbos, *J. Lumin.*, **111**, 89 (2005).
42. A. J. J. Bos, P. Dorenbos, A. Bessiere, A. Lecointre, M. Bedu, M. Bettinelli, and F. Piccinelli, *Rad. Meas.*, **46**, 1410 (2011).

43. Fangtian You, A. J. J. Bos, Qiufeng Shi, Shihua Huang, and P. Dorenbos, *Phys. Rev. B*, **85** 115101 (2012).
44. P. Dorenbos, *J. Lumin.*, **128**, 578 (2008).
45. P. Dorenbos, *J. Alloys and Compounds*, **488**, 568 (2009).
46. P. Dorenbos, *Phys. Rev. B*, **85**, 65107 (2012).
47. C. Pedrini, D. S. McClure, and C. H. Anderson, *J. Chem. Phys.*, **70**, 4959 (1979).
48. C. W. Thiel, Y. Sun, and R. L. Cone, *J. of Modern Optics*, **49**, 2399 (2002).
49. P. Dorenbos, *J. Lumin.*, **134**, 310 (2013).
50. J. Ueda, S. Tanabe, and T. Nakanishi, *J. Appl. Phys.*, **110**, 053102 (2011).